Smart Bandage With Wireless Strain and Temperature Sensors and Batteryless NFC Tag

Pablo Escobedo, Mitradip Bhattacharjee, *Member, IEEE*, Fatemeh Nikbakhtnasrabadi, and Ravinder Dahiya, *Fellow, IEEE*

***Abstract*—This article presents a smart bandage with wireless strain and temperature sensors and a batteryless near-field communication (NFC) tag. Both sensors are based on conductive poly (3,4-ethylenedioxythiophene) polystyrene sulfonate (PEDOT:PSS) polymer. The highly sensitive strain sensor consists of a microfluidic channel filled with PEDOT:PSS in Polydimethylsiloxane (PDMS) substrate. The strain sensor shows 3 order (∼1250) increase in the resistance for 10% strain and considerably high gauge factor (GF) of ∼12 500. The sensor was tested for ∼30% strain, which is more than typical stretching of human skin or body parts such as chest expansion during respiration. The strain sensor was also tested for different bending and the electrical resolution was ∼150% per degree of free bending and ∼12k% per percentage of stretching. The resistive temperature sensor, fabricated on a Polyvinyl Chloride (PVC) substrate, showed a ∼60% decrease in resistance when the temperature changed from 25 °C to 85 °C and a sensitivity of ∼1% per °C. As a proof of concept, the sensors and NFC tag were integrated on wound dressing to obtain wearable systems with smart bandage form factor. The sensors can be operated and read from distance of 25 mm with a user-friendly smartphone application developed for powering the system as well as real-time acquisition of sensors data. Finally, we demonstrate the potential use of smart bandage in healthcare applications such as assessment of wound status or respiratory diseases, such as asthma and COVID-19, where monitoring via wearable strain (e.g., respiratory volume) and temperature sensors is critical.**

***Index Terms*—Batteryless system, flexible electronics, near-field communication (NFC) tag, smart bandage, strain sensor, temperature sensor.**

I. Introduction

SENSOR-LADEN wearable systems have attracted huge interest in recent years because of the potential they hold for cost-effective self-health monitoring by allowing measurement of key health parameters and reducing the number of clinician contact hours [1]–[3]. As noninvasive means for health monitoring, these digital health solutions could improve the adherence of individuals to medical prescription [4]–[6]. As a result, several types of wearable sensors tethered to the patients via cables have been explored as an alternative to the traditional lab-based measurement systems [7]–[9]. These wearable systems capture compelling physiological data but, for greater acceptance, it is also crucial that they are nonobtrusive and, in this regard, there is also the need for integrating various types of sensors with low-power electronics and wireless radio communication interfaces on the same flexible and conformable substrate [10]–[13]. Herein, we present one such solution in a smart bandage form factor so that it conforms to the body, as shown in Fig. 1. The majority of such wearable systems have employed flexible sensors, but fully flexible or conformable systems, which also includes flexible electronics, are yet to come.

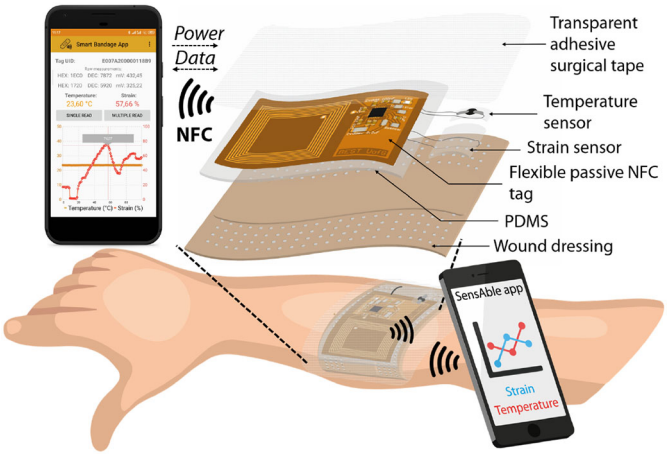

Fig. 1. Overview of the NFC-based smart bandage for wireless strain and temperature real-time monitoring. Powering and bidirectional communication is achieved by means of custom-developed smartphone application.

The smart bandage consists of two types of sensors (strain and temperature) and a batteryless near-field communication (NFC) tag to provide wirelessly the crucial information in applications such as of wound assessment [14]–[16]. A custom smartphone app was also developed to provide the required power to the sensing tag and make real-time measurements of both parameters. A few examples of smart bandages reported in literature for wound assessment are summarized in Table S1 in supplementary information (SI). They are based on monitoring parameters, such as pH [17]–[22],

Manuscript received November 1, 2020; revised December 9, 2020; accepted December 23, 2020. Date of publication December 30, 2020; date of current version March 5, 2021. This work was supported in part by the Engineering and Physical Sciences Research Council (EPSRC) through Engineering Fellowship for Growth under Grant EP/R029644/1, and in part by the North West Centre for Advanced Manufacturing (NW CAM) Project through the European Union's INTERREG VA Programme, managed by the Special EU Programmes Body (SEUPB) under Grant H2020-Intereg-IVA5055. *(Pablo Escobedo and Mitradip Bhattacharjee contributed equally to this work.) (Corresponding author: Ravinder Dahiya.)*

Pablo Escobedo, Fatemeh Nikbakhtnasrabadi, and Ravinder Dahiya are with the Bendable Electronics and Sensing Technologies Group, James Watt School of Engineering, University of Glasgow, Glasgow G12 8QQ, U.K. (e-mail: ravinder.dahiya@glasgow.ac.uk).

Mitradip Bhattacharjee is with the Bendable Electronics and Sensing Technologies Group, James Watt School of Engineering, University of Glasgow, Glasgow G12 8QQ, U.K., and also with the EECS, Indian Institute of Science Education and Research Bhopal, Bhopal 462066, India.

This article has supplementary downloadable material available at https://doi.org/10.1109/JIOT.2020.3048282, provided by the authors.

Digital Object Identifier 10.1109/JIOT.2020.3048282

temperature [23]–[25], uric acid [21], [26], moisture [27], oxygen [28], [29], lactate [29], pressure and strain [30]–[33], and others [14], [15], [34], [35]. However, none of these smart bandages is capable of measuring simultaneously the temperature and strain, even if they provide the crucial information about wound status. For example, temperature is a well-established marker of inflammation or infection in wounds and can be an early indicator of chronicity or predictor of healing even though wound appearances may not differ [15], [36]–[38]. Likewise, the skin strain can be used as an effective routine to keep track of wound closure or skin growth during wound healing [32], [39]–[41]. The application of controlled mechanical forces on a wound can also accelerate neovascularization and cellular proliferation, thus improving wound healing [42]. Thus, with strain and temperature sensors, the presented smart bandage addresses the need for simultaneous monitoring of the temperature and strain. In addition, the presented system could be useful for monitoring of respiratory diseases, such as asthma and COVID-19 [5], [43], [44], where wearable strain and temperature sensors could provide critical information, such as respiratory volume and body temperature [33], [45], [46]. The low-power device requirements [47], [48] in such IoT-based systems are desirable, and the proposed sensors were also fabricated keeping this in mind. The low-power consumption of the sensors and their interface means that they can directly operate from the energy acquired by the NFC harvester.

The presented system distinguishes from previous works by combining the following three main aspects simultaneously: 1) both the sensor and the electronics are integrated on flexible substrates; 2) it is able to measure simultaneously temperature and strain, two parameters that have been hardly ever combined so far for wound assessment; and 3) it implements wireless powering and data transmission using NFC technology, thus making the system compatible with any NFC-enabled smartphone through the custom-developed smartphone application. The data from sensors can be read and transmitted wirelessly by using technologies, such as radio-frequency identification (RFID), NFC, or Bluetooth. A key advantage of RFID/NFC technology over Bluetooth is the possibility of batteryless communication as the power required to operate sensors could be obtained with the electromagnetic (EM) field generated by a remote reader [49], [50]. NFC is a specialized subset within the family of RFID technology for short-range wireless systems. A distinct advantage of NFC over generic RFID lies in the peer-to-peer communication that can be achieved between an NFC-based system and any NFC-enabled smartphone acting as the remote reader, making this technology within the reach of any individual user.

II. Materials and Methods

A. Strain Sensor Design and Fabrication

Transparent polymer polydimethylsiloxane (PDMS) was used to fabricate the strain sensor [51]. In this case, the microchannel was realized in PDMS using replica molding technique. To this end, a 10:1 mixture of the PDMS and the cross-linker was prepared and mixed properly using a glass rod. The prepared mixture was then degassed for 1 h in a vacuum desiccator to remove all trapped air. Thereafter, the mixture was poured in a circular mould of diameter 5.5 cm. A metal wire (dia $\sim$275 μm) was used in the mould to create the microchannel inside the PDMS. The mould was then dried in a convection oven for 2 h at 70 °C. After drying, the cured PDMS was taken out of the mould and the wire was removed to obtain the microchannel. Thereafter, conducting liquid polymer PEDOT: PSS was injected into the microchannel using a syringe and it was then cured for another 3 h at 70 °C. The process of injection and curing was repeated three times. The optimization was done by measuring the electrical resistance of the sensor each time after the injection and curing cycle. After this, the fabricated sensor was cut into a rectangular shape of dimension (3 cm $\times$ 2 cm) for further experiments. Commercially available cylindrical Al electrodes with dia $\sim$275 μm were then inserted to both ends of the microchannel for electrical connections. A gap of $\sim$1.5 mm was kept inside the microchannel between the two electrodes.

B. Temperature Sensor Design and Fabrication

The flexible temperature sensor was fabricated using the conductive silver paint (RS 186-3600) on a commercial PVC substrate [52]. The PVC was cut into 2×2 cm pieces and two electrodes were formed using the Ag ink on the flexible PVC substrate using silver paste. The samples were then dried in a hot-air oven at 50 °C for 30 min. The gap between the two electrodes was $\sim$2 mm. Furthermore, a 10 μl of PEDOT:PSS was dispensed in the 2-mm gap using a micropipette. The samples were then dried at 50 °C for 1 h in an air oven. Thereafter, the samples were electrically characterized to evaluate the temperature response.

C. NFC Antenna Design and Characterization

The main electronic component in the smart bandage comprises is the NFC ISO15693 sensor transponder RF430FRL152H from Texas Instruments (Dallas, Texas, USA). Details about the design and fabrication of the flexible Printed Circuit Board (PCB) based on this transponder can be found in Section II of SI. This NFC chip is optimized for operation in a fully passive mode to develop batteryless designs in portable and wireless sensing applications. This is achieved by harvesting energy from the EM field induced by an external RFID reader, which in our case was an NFC-enabled smartphone. The custom antenna consists of a planar coil whose inductance was designed together with the internal capacitor value (C_{int}) of the RF430FRL152H IC to achieve resonance at 13.56 MHz, which is the central frequency required in the NFC protocol. Considering that resonance is achieved at $f_0 = 1/2\pi\sqrt{LC}$ and $C_{\text{int}} = 35$ pF at the frequency of interest, the inductance value required for the resonance of the tag is about 3.9 μH. However, to reduce the antenna dimensions, a $L_{\text{ant}} = 1.85\,\mu$H squared planar inductor was designed and an external capacitor of $C_{\text{ext}} = 39$ pF was placed in parallel to C_{int} to complete the resonant circuit. The initial inductance design was estimated through the Grover Method (see details in Section III of SI).

After the initial estimation, the final dimensions and number of turns for our antenna were obtained through the optimization process with EM simulation using COMSOL Multiphysics (COMSOL group, Stockholm, Sweden) and Advanced Design Simulator (ADS, Keysight Technologies, Santa Clara, CA, USA). As shown in Fig. 2(a), the final

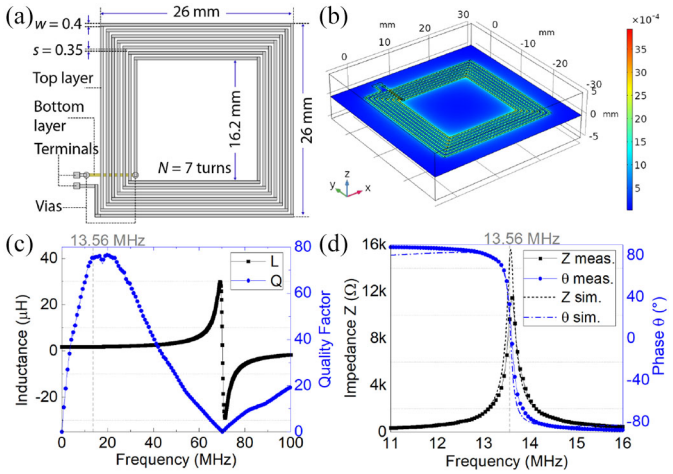

Fig. 2. (a) Geometric dimensions of the designed planar coil acting as NFC antenna. (b) Simulated magnetic flux density (T) and surface current density of the coil. (c) Measured frequency response of the fabricated planar inductor. (d) Simulated and measured impedance and phase of the parallel LC circuit after attaching the external capacitor and the RFID chip.

designed coil antenna had $N = 7$ turns with $w = 400$ μm as conductor width, $s = 350$ μm as the interspacing between the lines and overall dimensions of 26 mm^2. After fabrication, the frequency response of the antenna was measured using a precision impedance analyzer 4294A along with an impedance probe kit 4294A1 (Keysight Technologies, Santa Rosa, CA, USA). Fig. 2(b) depicts the simulated surface current density of the designed coil and the magnetic field around it, while Fig. 2(c) and (d) represents the frequency response of the antenna before and after attaching the external capacitor and the RFID chip. As observed in Fig. 2(c), a measured value of $L_{\text{ant}} = 1.816 \pm 0.004$ μH at 13.56 MHz was obtained, which is close to the designed inductance value. The measured quality factor at the same frequency was $Q = 74.9 \pm 0.3$. As shown in Fig. 2(d), after attaching the external capacitor and the chip, a maximum peak of resonance was achieved at 13.61 MHz, very close to the targeted resonant frequency of 13.56 MHz. To enable the use of an NFC-enabled smartphone as the external reader for both data communication and powering purposes, a user-friendly Android application (*SenseAble* app) was developed. Details and screenshots can be found in Section IV of SI. The supporting video (Movie S1 in SI) provides a demonstration of the working tag for strain and temperature measurement, including examples of the options available in the *SenseAble* application.

III. Results and Discussion

A. Strain Sensing

The developed strain sensor was characterized with a LabVIEW controlled strain generation setup, and measuring the electrical response using a digital multimeter (Agilent 34461A). The strain generation setup had two holders, which were able to move back and forth to generate uniaxial strain with controllable velocity in the sensor. The sensor was attached to the setup using the holders and thin metallic wires were used to make the electrical connections. A maximum of 30% strain was applied with a velocity of $V_S = 0.1$ mm/s. The strain sensor was tested for up to 30% of strain, which is

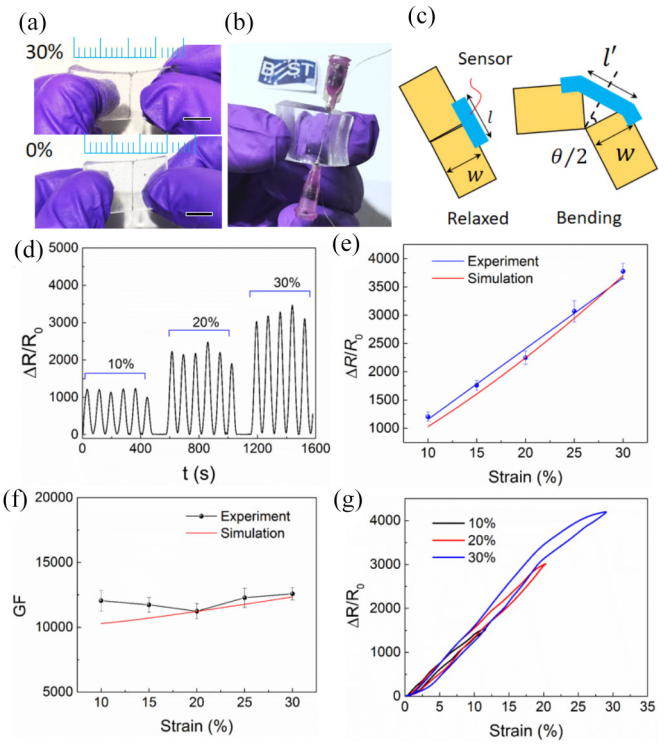

Fig. 3. (a) and (b) Image of the sensor at stretched, relaxed, and bending condition. (c) Schematic illustration of the sensor fixed on bendable support, such as robotic hand. (d) Response ($\Delta R/R_0$) of the sensor for different stretching (10%, 20%, and 30%) conditions. (e) Response of the sensor with strain values. (f) GF (experimental and simulated) of the strain sensor for different strain values. (g) Hysteresis curve of the fabricated strain sensor for different maximum strain values.

the typical strain limit associated with human skin at different body parts, such as fingers, wrists, knee, and elbows for the collagen fibres and tissues to become straitened [53], [54]. The real images and schematic diagram of the effect of bending are shown in Fig. 3(a)–(c), respectively. We observed three order ($\Delta R/R_0 \sim 1250$) of change in the electrical resistance of the sensor. The base resistance, in this case, was $\sim$140 Ω and the resistance at the highest strain was $\sim$180 kΩ. This is owing to the formation of defects and electrical discontinuities in the polymer as discussed in the following section. Fig. 3(c) shows the schematic illustration of the strain experienced by smart bandage during real-life use. If the user places the bandage on a body joint or in any part of the body, then the bending of the sensor will directly create a strain in the sensor and hence a bending of angle θ, as shown schematically in Fig. 3(c), would lead to stretching of $\Delta l = l' = 2w\sin(\theta/2)$, where l is the length of the sensor and w is the effective width of the bodypart. Hence, the correlation between the bending angle θ and stretching $\Delta l/l$ can be calculated using $\Delta l/l = l'/l = (2w\sin(\theta/2))/l$, which was used to calibrate the sensor.

Fig. 3(d) shows the temporal response of sensor for different stretching (10%, 20%, and 30%) conditions and Fig. 3(e) illustrates the response ($\Delta R/R_0$) of the sensor with respect to the applied strain. The electrical conductivity (σ) PEDOT:PSS in a microchannel depends on the volumetric fraction (V_f) of the defects and the percolation threshold [55], [56] or critical volumetric fraction of the filler (V_c) as $\sigma \propto (V_f - V_c)^s$, where variable s is the fitting parameter to best fit the experimental data. In this case, the effective V_f of polymer

PEDOT:PSS inside the channel reduces due to the deformation of the channel as it forms electrical discontinuities and defects. This can be explained by the electrical percolation mechanism [55]–[57].

The areal fraction of PEDOT:PSS is equal to the volumetric fraction of the materials, i.e., $V_f = D_f$ and $V_c = D_c$, where D_f and D_c are the corresponding areal fraction values, under the assumption of uniform distribution the PEDOT:PSS inside the PDMS microchannel. In this case, the expansion of microchannel due to applied strain results in the increase in electrical resistance of the sensor. The electrical conductivity, in this case, becomes $\sigma \propto (D_f - D_c)^s$ or $R \propto (D_f - D_c)^{-s}$ as the resistance and conductivity are inversely proportional [i.e., $R = (1/\sigma)(l/A)$, where l is the length of the conductor and A is the cross-sectional area].

In this case, the effective length and diameter of the channel were 1.5 mm and 175 μm, respectively. Furthermore, the number of electrical discontinuities in the system (N) and the magnitude of percentage strain ($\gamma = (\Delta L/L) \times 100$) in the sensor change the areal fraction D_f in the sensor. A linear relation $N = m\gamma + N_0$ was considered as the strain, in this case, was low [58], [59]. N_0 represents the initial electrical discontinuities present in the system; m ($= (E_1 \times A_1)/(E_2 \times A_2)$) is the proportionality constant; E_1 is the young's modulus of active material (i.e., PEDOT:PSS) and A_1 is a cross section of the channel, respectively; and E_2 and A_2 are the same parameters for embedded material (i.e., PDMS). The value of N_0 is negligible compared to the electrical discontinuities formed after the applied strain, whereas the value of m determines the formation of electrical discontinuities in the low strain region. Higher m signifies the higher crack formation for a particular strain value. Similarly, the percolation threshold can be given by $D_c = V_c = (\pi r^2 L)/(8\pi r^2 L + \pi r L^2)$, where L and r are the length and radius of the discontinuities, respectively. The theoretical results are in good agreement with the experimental values, as shown in Fig. 3(e). The value of the GF was measured (~12 000) and compared with the theoretical values in Fig. 3(f). The value of GF was considerably high compared to most of the previously reported resistive polymer strain sensors. Fig. 3(g) shows the hysteresis of the proposed strain sensor for 10%, 20%, and 30% maximum strain values. The hysteresis response shows that the sensor is considerably good for the smart-bandage application.

B. Temperature Sensing

Fig. 4(a) schematically shows the fabrication steps of the flexible temperature sensor as described in Section II-B. The sensor is based on the fact that PEDOT:PSS is sensitive to the temperature. The rise in temperature increases the rate of carrier mobility in the material and thus the resistance decreases.

The PEDOT:PSS-based temperature sensor was tested for a temperature range of 25 °C–85 °C, which covers typical temperatures at wound sites [25], [60], [61]. Despite a large range of operation, the sensor will mostly operate in the range of 30 °C–50 °C. In this case, the skin temperature around the wound could be a potential indicator of the wound status. The sensor was characterized using a hotplate having a digital display and a LabVIEW-enabled digital multimeter. The temperature sensitive PEDOT:PSS with two Ag electrodes was placed on the digital hotplate and the temperature was varied from 25°C to 80 °C. It was found that the resistance was decreasing with the increase in temperature, as illustrated in Fig. 4(b). The sensor was left for some time to saturate before the temperature of the hotplate underneath was increased to a higher value. The resistance decreases and reaches a stable state in about 5–8 s for a temperature increase of ~5 °C from 40 °C to 45 °C, as shown in Fig. 4(c). Furthermore, the sensor was exposed to different temperatures and the response (R/R_0) was recorded. Fig. 4(d) shows the change in R/R_0 with temperature and Fig. 4(e) shows the same for normalized conductance (σ/σ_0). In this case, the change in normalized conductance showed a good quadratic fit with the variation in temperature. The dependence of conductance with temperature can be expressed as a second-order equation $Y = ax^2 + bx + c$, as shown in Fig. 4(e), where $a = 3.8 \times 10^{-4}$, $b = 0.66 \times 10^{-4}$, and $c = 0.51$. In the literature also, a quadratic relation between resistance and temperature has been previously reported [62], [63]. However, the resistance, in this case, is linear with temperature ($Y = mx + c'$) as shown in Fig. 4(d), where $m = 7.4 \times 10^{-3}$ and $c' = 1.12$. The resistance changed about 45 Ω for a change of 5 °C from 40 °C to 45 °C, while the noise was ~2.2%. This value was calculated by measuring the fluctuations of response from the linear fit and the temperature resolution, i.e., the minimum difference between two detectable consecutive temperature values was calculated to be ~2 °C.

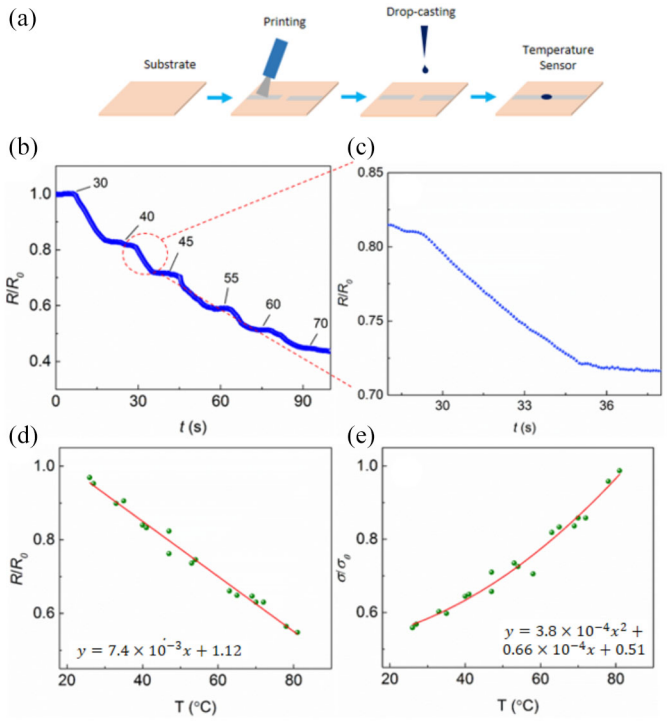

Fig. 4. (a) Schematic illustration of the fabrication steps of the flexible temperature sensor. (b) Change in the sensor response (R/R_0) with time (t). (c) Response (R/R_0) of the sensor for temperature increase of ~5 °C, from 40 °C to 45 °C. (d) Response of sensor at different temperature values (T). (e) Change in normalized conductance (σ/σ_0) with temperature.

C. Smart Bandage Design and Operation

The circuit and system-level block diagrams of the developed smart bandage system are shown in Fig. 5(a)

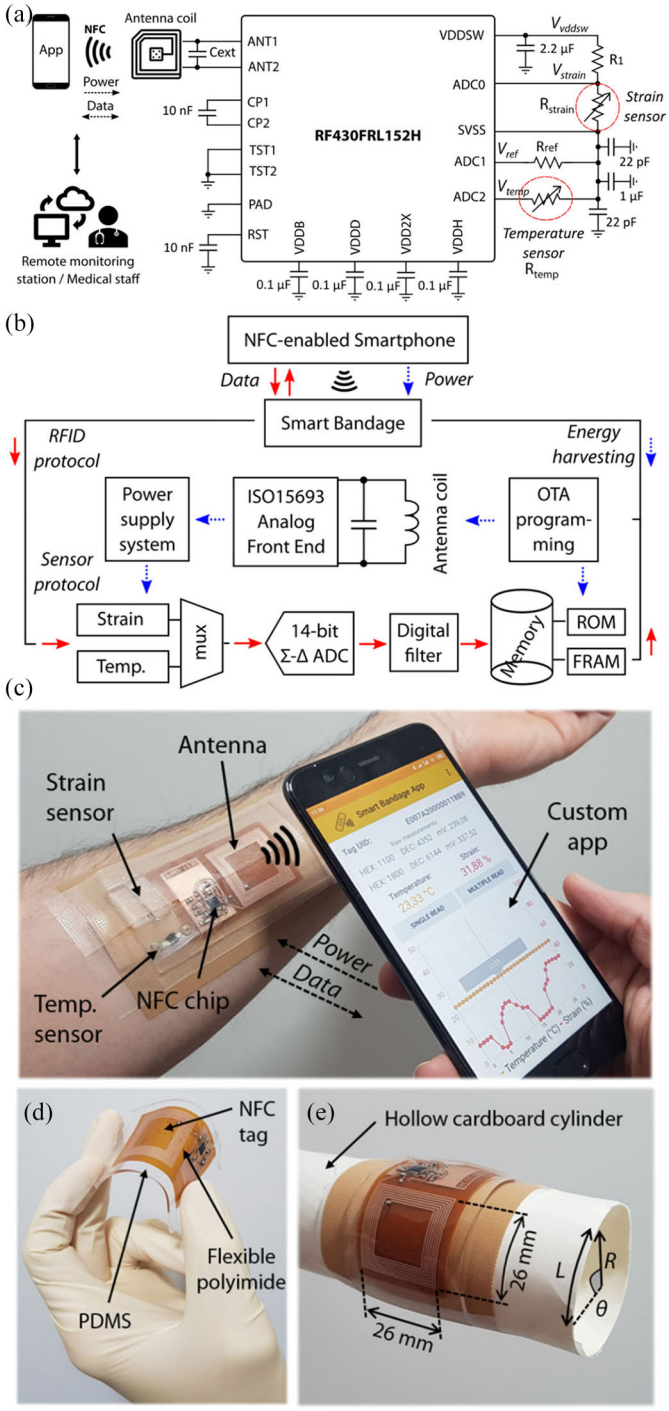

Fig. 5. (a) Circuit and system level. (b) Block diagram of the developed smart bandage for wireless strain and temperature monitoring. (c) Photographs of the NFC-based smart bandage attached on the arm as a proof of concept for wireless strain and temperature monitoring using the custom smartphone application. (d) NFC tag fabricated in flexible polyimide and embedded in PDMS. (e) Smart bandage attached on hollow cardboard cylinder for the bending tests.

and (b), respectively. The RF430FRL152H transponder was used as the interface between the two sensors and the *SenseAble* smartphone application for sensor data acquisition and transmission. For that purpose, two different interfaces were needed. The ISO/IEC 15693 compliant RFID interface was used for wireless programming, configuration, and bidirectional data communication. To achieve this, the designed flexible loop antenna was connected to the RF analogue front end of the chip using ANT1 and ANT2 pins. The batteryless operation of the smart bandage was achieved through EM energy harvesting upon the approach of the RFID reader, which in our case was an NFC-enabled smartphone running the custom application *SenseAble*. Since both the strain and temperature sensors do not require any external power for their operation, the harvested energy was used only to power the chip and its internal functional blocks. The interface between the sensors and the RF430FRL152H transponder was done through a resistive sensor bias interface, which uses an internal 14-b sigma–delta analogue-to-digital converter (ADC) and a programmable gain amplifier (PGA) featuring a very high-impedance input and a programmable gain combined with full offset compensation, very low offset drift, and low noise. As shown in Fig. 5(a), a voltage divider was implemented as the conditioning circuit for strain sensor. One end of the resistor R_1 was connected to VDDSW, a regulated output voltage of $V_{\text{ddsw}} \sim 1.5$ V with a current up to 450 μA (i.e., $\sim$675 μW) that the chip can provide with an adequate EM field from the RFID reader. The other end of R_1 was connected to the strain sensor (R_{strain}) and one of the analogue-to-digital converter inputs (ADC0). The other terminal of R_{strain} was grounded to SVSS with the virtual ground setting enabled on the chip. Using this option, the voltage at SVSS is raised to approximately 125 mV to prevent minor errors due to the nonlinear behavior of the ADC near the ground. More details regarding the implementation of the circuit for the strain acquisition can be found in Section V of SI.

The temperature sensor (R_{temp}) was connected between ADC2 and SVSS. To get more accurate temperature measurements, a reference resistor ($R_{\text{ref}} = 100$ kΩ) was also used and connected between ADC1 and SVSS. The temperature measurement approach was different from the strain sensing in that a current source was applied to the temperature sensor (ADC2) and reference (ADC1) pins to determine their resistances. Typically, an output current of $\sim$2.4 μA is applied by the chip to both pins according to the specifications, but the exact amperage of this current source can vary from device to device. Using the known resistor R_{ref}, the accurate current level through both pins can be determined, and thus a precise voltage calculation can be performed. Section IV in SI contains more details regarding the procedure for the temperature sensing acquisition and calculations. For the sampling of both sensors, a digital decimation filter was programmed after the 14-b sigma–delta converter to achieve noise reduction. It consisted of a cascaded integrator-comb (CIC) filter whose decimation ratio was programmed to 256. This resulted in a conversion time of 128 ms, which was quick enough for our application. The chip was programmed to sequentially sample the voltage values at the three ADC pins, storing them in specific locations of the FRAM. Those memory locations were then accessed by the *SenseAble* application through NFC commands, and the voltage values were converted to strain and temperature values using the above-mentioned calibrations. To develop the program that conducts the readout routine in the chip, code composer studio (CCS) version 7.4 was used. The firmware was uploaded to the RF430FRL152H ROM using over the air programming (OTA) through a TRF7970A RFID reader from Texas Instruments.

As a proof of concept, Fig. 5(c) shows a photograph of the complete system attached on a human arm, where the flexible passive tag [Fig. 5(d)] has been integrated along with the temperature and strain sensors in a standard wound dressing. The transparent adhesive surgical tape was used to protect the whole structure from the environment. Given the modular design of the system, the temperature and strain sensors can be placed at different and more convenient locations than the ones showed in the photograph, thus adapting to the specific requirements in each case. For instance, the temperature sensor could be placed below the wound dressing to get more in contact with the skin. The supporting video (Movie S1 in SI) provides demonstrations of the working tag for strain and temperature monitoring and its operation with the custom developed *SenseAble* smartphone application.

The typical reading distance of an NFC tag is between 1 and 5 cm if the tag is scanned with a mobile phone as a reader. Several factors can affect the performance, including the technology within the NFC chip, the tag antenna size and design, the tag quality, and the reader antenna. In flat position and with the Xiaomi Mi6 smartphone used in this work (Xiaomi Inc., Beijing, China), a maximum vertical reading distance of 43 mm was achieved. Several curvatures were tested to study their impact on the tag's reading distance. For that purpose, the tag was bent by fitting it to the convex surfaces of hollow cardboard cylinders with different radii (R). Selected cylinder radii were $R = 100$, 50, 20, and 10 mm. As an example, Fig. 5(e) shows the case of $R = 20$ mm. The bending angle (θ) in radians can be calculated as the component's length in the curvature direction (L) divided by the cylinder radius (R). The length was considered to be $L = 26$ mm, which is the size of the designed squared antenna. Therefore, for the selected radii the bending angles were in the range from $\sim 15°$ up to $\sim 150°$. These values are equivalent to the bending required to conform to human limbs, for example, $R = 100$ and 20 mm are equivalent to the approximate curvature of an adult thigh and finger respectively. The reading distance was reduced with the bending radius, being 40 mm for the case $R = 100$ mm down to 23 mm for $R = 10$ mm. In the intermediate cases of $R = 50$ and 20 mm, the measured reading distances were 35 and 32 mm, respectively. Although the previous results were taken off body, no major differences were observed in the reading distance when the tag was attached to different human body parts. For instance, maximum reading distances of 41, 38, and 25 mm were measured with the tag attached to a thigh, a wrist, and a thumb, respectively.

Finally, the smart bandage was tested as a proof of concept on a medical anatomic mannequin for wireless monitoring of chest expansion and contraction during respiration using the strain sensor [64], [65]. This can be of particular interest for wireless assessment of respiratory diseases, such as asthma and COVID-19. For that purpose, the smart bandage was placed on the chest of a cardiopulmonary resuscitation (CPR) manikin, as observed in Fig. 6(a). The CPR manikin was used in conjunction with GlasVent, which is a low cost, emergency, Do it Yourself (DIY) ventilator developed by our group [44]. As shown in Fig. 6(a), GlasVent is an automated version of manual resuscitator device commonly known as bag mask ventilation (BVM or AMBU bag), which is widely used by clinicians prior to initiating the mechanical ventilation. With the smart bandage fixed to the chest, respiration could be wirelessly monitored using the *SenseAble* app by the upward and downward slopes of the relative resistance associated with inhalation and exhalation (chest expansion and contraction), as observed in Fig. 6(b) and (c). The supporting video (Movie S2 in SI) provides demonstration of the real-time wireless monitoring of chest expansion and contraction during respiration using the developed smart bandage and GlasVent on a CPR manikin

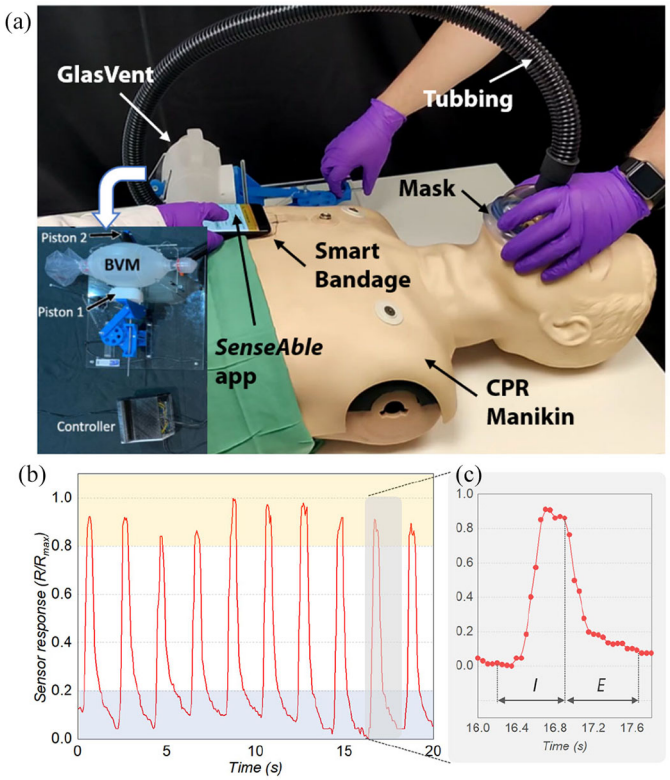

Fig. 6. (a) Experimental setup for the wireless monitoring of chest expansion and contraction during respiration using the smart bandage and the GlasVent ventilator in medical CPR manikin. (b) Sensor response over time measured by the smart bandage associated with the inspiration and expiration cycles during respiration. In this case, the resistance of the strain sensor was normalized to the maximum resistance obtained during the chest expansion due to inhalation. (c) Detailed view of one breath cycle consisting of two-time components, i.e., inspiration (I) and expiration (E).

IV. Conclusion

In summary, a flexible and conformable smart bandage is presented for wireless strain and temperature sensing. Both strain and temperature sensors were integrated with a batteryless NFC tag based on a flexible polyimide substrate. The PEDOT:PSS polymer-based sensors are disposable and demonstrated considerably good performance for this application. The microchannel-based strain sensor was fabricated using PDMS and PEDOT:PSS and it showed an average GF ($\mathrm{GF} = (\Delta R/R_0)/(\Delta L/L)$) of $\sim$12 500, which is considerably high for this application. An electrical resolution of $\sim$150% per degree of free bending and $\sim$12k% per percentage of stretching was observed for the said strain sensor. Similarly, the PEDOT:PSS-based temperature sensor showed a $\sim$70% decrease in resistance for a temperature change from 25 °C to 90 °C with a sensitivity of $\sim$1.2% for each °C change in temperature. Furthermore, the proposed tag was batteryless

and was powered using the EM field from a standard NFC-enabled smartphone. The sensor real-time data was recorded and processed using a user-friendly custom-developed smartphone application—the SenseAble app. The tag was also integrated with a standard wound dressing. The minimum reading distance of ∼25 mm was achieved after the smart bandage attached to the human limb. However, the maximum reading distance was observed to be ∼43 mm for the tag in flat position. This tag can be used in different healthcare applications for wirelessly monitoring of wound status or respiratory diseases, such as asthma and COVID-19, where monitoring via wearable strain (e.g., respiratory volume) and temperature sensors is critical.

ACKNOWLEDGMENT

The views and opinions in this document do not necessarily reflect those of the European Commission or the SEUPB.

REFERENCES

[1] W. Gao, H. Ota, D. Kiriya, K. Takei, and A. Javey, "Flexible electronics toward wearable sensing," *Accounts Chem. Res.*, vol. 52, no. 3, pp. 523–533, 2019.

[2] S. Nasiri and M. R. Khosravani, "Progress and challenges in fabrication of wearable sensors for health monitoring," *Sens. Actuat. A*, vol. 312, Sep. 2020, Art. no. 112105.

[3] I. Sim, "Mobile devices and health," *New England J. Med.*, vol. 381, no. 10, pp. 956–968, 2019.

[4] M. S. Brown, B. Ashley, and A. Koh, "Wearable technology for chronic wound monitoring: Current dressings, advancements, and future prospects," *Front. Bioeng. Biotechnol.*, vol. 6, p. 47, Apr. 2018.

[5] P. Sharma, X. Hui, J. Zhou, T. B. Conroy, and E. C. Kan, "Wearable radio-frequency sensing of respiratory rate, respiratory volume, and heart rate," *NPJ Digit. Med.*, vol. 3, no. 1, p. 98, 2020.

[6] H. Wang *et al.*, "Guest editorial: Special issue on Internet of Things for smart and connected health," *IEEE Internet Things J.*, vol. 2, no. 1, pp. 1–4, Feb. 2015.

[7] J. Kim, A. S. Campbell, B. E.-F. de Ávila, and J. Wang, "Wearable biosensors for healthcare monitoring," *Nat. Biotechnol.*, vol. 37, no. 4, pp. 389–406, 2019.

[8] Y. Liu, H. Wang, W. Zhao, M. Zhang, H. Qin, and Y. Xie, "Flexible, stretchable sensors for wearable health monitoring: Sensing mechanisms, materials, fabrication strategies and features," *Sensors*, vol. 18, no. 2, p. 645, 2018.

[9] P. Escobedo *et al.*, "Smartphone-based diagnosis of parasitic infections with colorimetric assays in centrifuge tubes," *IEEE Access*, vol. 7, pp. 185677–185686, 2019.

[10] M. Bhattacharjee, S. Middya, P. Escobedo, J. Chaudhuri, D. Bandyopadhyay, and R. Dahiya, "Microdroplet based disposable sensor patch for detection of α-amylase in human blood serum," *Biosens. Bioelectron.*, vol. 165, Oct. 2020, Art. no. 112333.

[11] P. Kassal, M. D. Steinberg, and I. M. Steinberg, "Wireless chemical sensors and biosensors: A review," *Sens. Actuat. B, Chem.*, vol. 266, pp. 228–245, Aug. 2018.

[12] Y. Liu, M. Pharr, and G. A. Salvatore, "Lab-on-skin: A review of flexible and stretchable electronics for wearable health monitoring," *ACS Nano*, vol. 11, no. 10, pp. 9614–9635, 2017.

[13] X. Wang, Z. Liu, and T. Zhang, "Flexible sensing electronics for wearable/attachable health monitoring," *Small*, vol. 13, no. 25, 2017, Art. no. 1602790.

[14] H. Derakhshandeh, S. S. Kashaf, F. Aghabaglou, I. O. Ghanavati, and A. Tamayol, "Smart bandages: The future of wound care," *Trends Biotechnol.*, vol. 36, no. 12, pp. 1259–1274, 2018.

[15] T. R. Dargaville, B. L. Farrugia, J. A. Broadbent, S. Pace, Z. Upton, and N. H. Voelcker, "Sensors and imaging for wound healing: A review," *Biosens. Bioelectron.*, vol. 41, pp. 30–42, Mar. 2013.

[16] E. S. Hosseini, M. Bhattacharjee, L. Manjakkal, and R. Dahiya, "Healing and monitoring of chronic wounds: Advances in wearable technologies," in *From A to Z: Wearables in Modern Medicine*, S. Stuart and A. Godfrey, Eds., Academic Press, London, U.K.: Elsevier, 2021.

[17] P. Kassal, M. Zubak, G. Scheipl, G. J. Mohr, M. D. Steinberg, and I. M. Steinberg, "Smart bandage with wireless connectivity for optical monitoring of pH," *Sens. Actuat. B, Chem.*, vol. 246, pp. 455–460, Jul. 2017.

[18] R. Rahimi *et al.*, "Laser-enabled fabrication of flexible and transparent pH sensor with near-field communication for in-situ monitoring of wound infection," *Sens. Actuat. B, Chem.*, vol. 267, pp. 198–207, Aug. 2018.

[19] W. Dang, L. Manjakkal, W. T. Navaraj, L. Lorenzelli, V. Vinciguerra, and R. Dahiya, "Stretchable wireless system for sweat pH monitoring," *Biosens. Bioelectron.*, vol. 107, pp. 192–202, Jun. 2018.

[20] T. Guinovart, G. Valdés-Ramírez, J. R. Windmiller, F. J. Andrade, and J. Wang, "Bandage-based wearable potentiometric sensor for monitoring wound pH," *Electroanalysis*, vol. 26, no. 6, pp. 1345–1353, 2014.

[21] A. Pal, D. Goswami, H. E. Cuellar, B. Castro, S. H. Kuang, and R. V. Martinez, "Early detection and monitoring of chronic wounds using low-cost, omniphobic paper-based smart bandages," *Biosensors. Bioelectron.*, vol. 117, pp. 696–705, Oct. 2018.

[22] M. F. Farooqui and A. Shamim, "Low cost inkjet printed smart bandage for wireless monitoring of chronic wounds," *Sci. Rep.*, vol. 6, Jun. 2016. Art. no. 28949.

[23] P. Mostafalu *et al.*, "Smart bandage for monitoring and treatment of chronic wounds," *Small*, vol. 14, no. 33, 2018, Art. no. e1703509.

[24] D. P. Rose *et al.*, "Adhesive RFID sensor patch for monitoring of sweat electrolytes," *IEEE Trans. Biomed. Eng.*, vol. 62, no. 6, pp. 1457–1465, Jun. 2015.

[25] Q. Pang *et al.*, "Smart flexible electronics-integrated wound dressing for real-time monitoring and on-demand treatment of infected wounds," *Adv. Sci.*, vol. 7, no. 6, 2020, Art. no. 1902673.

[26] P. Kassal *et al.*, "Smart bandage with wireless connectivity for uric acid biosensing as an indicator of wound status," *Electrochem. Commun.*, vol. 56, pp. 6–10, Jul. 2015.

[27] S. D. Milne *et al.*, "A wearable wound moisture sensor as an indicator for wound dressing change: An observational study of wound moisture and status," *Int. Wound J.*, vol. 13, no. 6, pp. 1309–1314, 2016.

[28] P. Mostafalu, W. Lenk, M. R. Dokmeci, B. Ziaie, A. Khademhosseini, and S. R. Sonkusale, "Wireless flexible smart bandage for continuous monitoring of wound oxygenation," *IEEE Trans. Biomed. Circuits Syst.*, vol. 9, no. 5, pp. 670–677, Oct. 2015.

[29] B. K. Ashley, M. S. Brown, Y. Park, S. Kuan, and A. Koh, "Skin-inspired, open mesh electrochemical sensors for lactate and oxygen monitoring," *Biosens. Bioelectron.*, vol. 132, pp. 343–351, May 2019.

[30] E. S. Hosseini, L. Manjakkal, D. Shakthivel, and R. Dahiya, "Glycine–chitosan-based flexible biodegradable piezoelectric pressure sensor," *ACS Appl. Mater. Interfaces*, vol. 12, no. 8, pp. 9008–9016, 2020.

[31] W.-J. Deng, L.-F. Wang, L. Dong, and Q.-A. Huang, "LC wireless sensitive pressure sensors with microstructured PDMS dielectric layers for wound monitoring," *IEEE Sensors J.*, vol. 18, no. 12, pp. 4886–4892, Jun. 2018.

[32] J. Zhang, Y. Li, and Y. Xing, "Ultrasoft, adhesive and millimeter scale epidermis electronic sensor for real-time enduringly monitoring skin strain," *Sensors (Basel)*, vol. 19, no. 11, p. 2442, 2019.

[33] M. Chu *et al.*, "Respiration rate and volume measurements using wearable strain sensors," *NPJ Digit. Med.*, vol. 2, p. 8, Feb. 2019.

[34] M. A. Kafi, A. Paul, A. Vilouras, E. S. Hosseini, and R. S. Dahiya, "Chitosan-graphene oxide-based ultra-thin and flexible sensor for diabetic wound monitoring," *IEEE Sensors J.*, vol. 20, no. 13, pp. 6794–6801, Jul. 2020.

[35] M. Ochoa, R. Rahimi, and B. Ziaie, "Flexible sensors for chronic wound management," *IEEE Rev. Biomed. Eng.*, vol. 7, pp. 73–86, Dec. 2013.

[36] G. Nakagami *et al.*, "Predicting delayed pressure ulcer healing using thermography: A prospective cohort study," *J. Wound Care*, vol. 19, no. 11, pp. 465–466, 2010.

[37] M. A. Martinez-Jimenez *et al.*, "Local use of insulin in wounds of diabetic patients: Higher temperature, fibrosis, and angiogenesis," *Plast. Reconstruct. Surg.*, vol. 132, no. 6, pp. 1015e–1019e, 2013.

[38] D. P. Cuthbertson and W. J. Tilstone, "Effect of environmental temperature on the closure of full thickness skin wounds in the rat," *Quart. J. Exp. Physiol. Cogn. Med. Sci.*, vol. 52, no. 3, pp. 249–257, 1967.

[39] S. O. Blacklow, J. Li, B. R. Freedman, M. Zeidi, C. Chen, and D. J. Mooney, "Bioinspired mechanically active adhesive dressings to accelerate wound closure," *Sci. Adv.*, vol. 5, no. 7, p. eaaw3963, 2019.

[40] R. Agha, R. Ogawa, G. Pietramaggiori, and D. P. Orgill, "A review of the role of mechanical forces in cutaneous wound healing," *J. Surg. Res.*, vol. 171, no. 2, pp. 700–708, 2011.

[41] J. D. Urschel, P. G. Scott, and H. T. Williams, "The effect of mechanical stress on soft and hard tissue repair; a review," *Brit. J. Plast. Surg.*, vol. 41, no. 2, pp. 182–186, 1988.
[42] E. J. F. Timmenga, T. T. Andreassen, H. J. Houthoff, and P. J. Klopper, "The effect of mechanical stress on healing skin wounds: An experimental study in rabbits using tissue expansion," *Brit. J. Plast. Surg.*, vol. 44, no. 7, pp. 514–519, 1991.
[43] J. J. Marini and L. Gattinoni, "Management of COVID-19 respiratory distress," *J. Amer. Med. Assoc.*, vol. 323, no. 22, pp. 2329–2330, 2020.
[44] A. Christou, M. Ntagios, A. Hart, and R. Dahiya, "GlasVent—The rapidly deployable emergency ventilator," *Global Challenges*, vol. 4, no. 12, 2020, Art. no. 2000046.
[45] M. Cao *et al.*, "Clinical features of patients infected with the 2019 novel coronavirus (COVID-19) in Shanghai, China," medRxiv, 2020, doi: 10.1101/2020.03.04.20030395.
[46] S. Tharakan, K. Nomoto, S. Miyashita, and K. Ishikawa, "Body temperature correlates with mortality in COVID-19 patients," *Crit. Care*, vol. 24, no. 1, p. 298, 2020.
[47] S. Lee and A. Nathan, "Subthreshold Schottky-barrier thin-film transistors with ultralow power and high intrinsic gain," *Science*, vol. 354, no. 6310, pp. 302–304, 2016.
[48] C. Jiang, H. W. Choi, X. Cheng, H. Ma, D. Hasko, and A. Nathan, "Printed subthreshold organic transistors operating at high gain and ultralow power," *Science*, vol. 363, no. 6428, pp. 719–723, 2019.
[49] P. Escobedo *et al.*, "General-purpose passive wireless point–of–care platform based on smartphone," *Biosens. Bioelectron.*, vol. 141, Sep. 2019, Art. no. 111360.
[50] P. Escobedo *et al.*, "Flexible passive near field communication tag for multigas sensing," *Anal. Chem.*, vol. 89, no. 3, pp. 1697–1703, 2017.
[51] M. Bhattacharjee, M. Soni, P. Escobedo, and R. Dahiya, "PEDOT:PSS microchannel-based highly sensitive stretchable strain sensor," *Adv. Electron. Mater.*, vol. 6, Aug. 2020, Art. no. 2000445.
[52] M. Soni, M. Bhattacharjee, M. Ntagios, and R. Dahiya, "Printed temperature sensor based on PEDOT: PSS-graphene oxide composite," *IEEE Sensors J.*, vol. 20, no. 14, pp. 7525–7531, Jul. 2020.
[53] H. Joodaki and M. B. Panzer, "Skin mechanical properties and modeling: A review," *Proc. Inst. Mech. Eng. Med.*, vol. 232, no. 4, pp. 323–343, 2018.
[54] A. B. Tepole, A. K. Gosain, and E. Kuhl, "Stretching skin: The physiological limit and beyond," *Int. J. Nonlinear Mech.*, vol. 47, no. 8, pp. 938–949, 2012.
[55] M. Park *et al.*, "Highly stretchable electric circuits from a composite material of silver nanoparticles and elastomeric fibres," *Nat. Nanotechnol.*, vol. 7, no. 12, pp. 803–809, 2012.
[56] J. Li and J.-K. Kim, "Percolation threshold of conducting polymer composites containing 3D randomly distributed graphite nanoplatelets," *Compos. Sci. Technol.*, vol. 67, no. 10, pp. 2114–2120, 2007.
[57] S. I. White *et al.*, "Electrical percolation behavior in silver nanowire–polystyrene composites: Simulation and experiment," *Adv. Funct. Mater.*, vol. 20, no. 16, pp. 2709–2716, 2010.
[58] V. B. Shenoy, A. F. Schwartzman, and L. B. Freund, "Crack patterns in brittle thin films," *Int. J. Fract.*, vol. 109, no. 1, pp. 29–45, 2001.
[59] Z. C. Xia and J. W. Hutchinson, "Crack patterns in thin films," *J. Mech. Phys. Solids*, vol. 48, nos. 6–7, pp. 1107–1131, 2000.
[60] V. Dini, P. Salvo, A. Janowska, F. Di Francesco, A. Barbini, and M. Romanelli, "Correlation between wound temperature obtained with an infrared camera and clinical wound bed score in venous leg ulcers," *Wounds*, vol. 27, no. 10, pp. 274–278, 2015.
[61] M. Fierheller and R. G. Sibbald, "A clinical investigation into the relationship between increased periwound skin temperature and local wound infection in patients with chronic leg ulcers," *Adv. Skin Wound Care*, vol. 23, no. 8, pp. 369–379, 2010.
[62] S. Vihodceva, A. Ramata-Stunda, and A. Pumpure, "Evaluation of dermal toxicity of antibacterial cotton textile coated by sol-gel technology," *J. Text. Inst.*, vol. 109, no. 7, pp. 961–966, 2018.
[63] T. Zandt, H. Dwelk, C. Janowitz, and R. Manzke, "Quadratic temperature dependence up to 50 K of the resistivity of metallic $MoTe_2$," *J. Alloy. Comp.*, vol. 442, nos. 1–2, pp. 216–218, 2007.
[64] T. Yamada *et al.*, "A stretchable carbon nanotube strain sensor for human-motion detection," *Nat. Nanotechnol.*, vol. 6, no. 5, pp. 296–301, 2011.
[65] A. Yamamoto *et al.*, "Monitoring respiratory rates with a wearable system using a stretchable strain sensor during moderate exercise," *Med. Biol. Eng. Comput.*, vol. 57, no. 12, pp. 2741–2756, 2019.

Pablo Escobedo received the first M.Sc. degree in telecommunication engineering, the second M.Sc. degree in electronics engineering, and the master's degree in computer and network engineering from the University of Granada (UGR), Granada, Spain, in 2012, 2013, and 2014, respectively, and the Ph.D. degree from ECSens Group, UGR in 2018.

He is currently a Postdoctoral Researcher with the Bendable Electronics and Sensing Technologies Group, University of Glasgow, Glasgow, U.K. His research includes the development of printed sensor systems on flexible substrates, with special interest in smart tags with RFID/NFC technology for environmental, health and food quality monitoring applications, and electronic skin for applications in the fields of robotics, prosthetics, health diagnostics, and wearables.

Mitradip Bhattacharjee (Member, IEEE) received the B.Tech. degree in electronics and communication engineering from the National Institute of Technology Agartala, Agartala, India, in 2013, and the Ph.D degree from the Indian Institute of Technology Guwahati, Guwahati, India, in December 2018.

He is currently an Assistant Professor with the Electrical Engineering and Computer Science Department, Indian Institute of Science Education and Research Bhopal, Bhopal, India. He joined the Bendable Electronics and Sensing Technologies Group, University of Glasgow, Glasgow, U.K., as a Postdoctoral Fellow in January 2019. His research interests include electronic sensors and systems, biomedical engineering, bioelectronics, flexible/printed and wearable electronics, wireless systems, and reconfigurable sensing antenna.

Fatemeh Nikbakhtnasrabadi received the B.Sc. degree in electrical engineering and the M.Sc. degree in telecommunication engineering from Shahed University, Tehran, Iran, in 2010 and 2013, respectively. She is currently pursuing the Ph.D. degree from the Electronics and Nanoscale Division, Bendable Electronics and Sensing Technologies Group, University of Glasgow, Glasgow, U.K.

Her research interests include design of antennas and RFIDs for healthcare application and smart labeling.

Ravinder Dahiya (Fellow, IEEE) received PhD in humanoid technologies from University of Genoa, Italy and Istituto Italiano di Tecnologia, Genoa, Italy in 2009. He is currently a Professor of Electronics and Nanoengineering with the University of Glasgow, Glasgow, U.K. He is the Leader of Bendable Electronics and Sensing Technologies Research Group, which conducts fundamental and applied research in flexible electronics, tactile sensing, electronic skin, robotics, and wearable systems. He has authored over 350 research articles, seven books, and 15 submitted/granted patents. He has led several international projects.

Prof. Dahiya has received several awards, including the 2016 Microelectronic Engineering Young Investigator Award (Elsevier), the 2016 Technical Achievement Award from the IEEE Sensors Council, and 9 Best Paper awards as authored/coauthored in International Conferences and Journals. He holds the prestigious EPSRC Fellowship and received in past the Marie Curie and Japanese Monbusho Fellowships. He was the Technical Program Co-Chair of IEEE SENSORS CONFERENCE in 2017 and 2018, and has been a General Chair of several conferences, including IEEE International Conference on Flexible and Printable Sensors and Systems in 2019, 2020, and 2021, which he founded. He was also on the editorial boards of IEEE SENSORS JOURNAL from 2012 to 2020 and IEEE TRANSACTIONS ON ROBOTICS from 2012 to 2017. He is the President-Elect Distinguished Lecturer of the IEEE Sensors Council and is serving on the editorial boards of the Scientific Report.